Check for updates

Nb$_2$C Mxene as a bifunctional acid–base and oxidation/hydrogenation catalyst†

Octavian Pavel, [a] Alina Tirsoaga,[a] Bogdan Cojocaru,[a] Dana Popescu,[ac]
Ruben Ramírez-Grau,[b] Pablo González-Durán, [b] Pablo García-Aznar, [b]
Liang Tian, [b] German Sastre, [b] Ana Primo,*[b] Vasile Parvulescu [*a] and
Hermenegildo Garcia [b]

Nb$_2$C MXene, obtained from Nb$_2$AlC by Al^{3+} etching and exfoliation, was characterized using XRD, HRTEM and AFM, with the data confirming the crystallinity of the sample and the 2D morphology of the sheets with an average layer thickness of 1.5 nm. Surface analysis using XPS revealed the presence of structural defects, and NH$_3$- and CO$_2$-TPD profiles confirmed the low density of acid and basic sites in the range of tens of μmol g$_{catalyst}^{-1}$ of weak and moderate strengths. The combination of acid and basic sites in close proximity on the solid surface was responsible for the remarkable catalytic activity of Nb$_2$C MXene in promoting aldolic condensation with high turnover frequencies of up to 855 h^{-1}, which was comparable to the values of benchmark catalysts, such as MgO or HZSM-5. Nb$_2$C MXene also catalyzed the aerobic oxidative aniline coupling to azo- and azoxy-benzene and hydrogenation of azoxybenzene to azobenzene.

Broader context

In heterogeneous catalysis, there is a constant search for new materials with improved performance and selectivity to drive chemical reactions. In this study, we demonstrate that Nb$_2$C, a member of the MXene family, can function as a bifunctional acid–base catalyst, effectively promoting aldol condensation reactions, as well as an aerobic oxidation catalyst by activating molecular oxygen. Both reaction types are of broad interest in organic synthesis. The turnover frequencies achieved with Nb$_2$C rank it among the most active solid catalysts for these processes. Characterization and modeling indicate that the active sites are atomic vacancies in the Nb$_2$C structure created during its synthesis. The broader impact of this study is that MXenes offer a vast chemical space and can be fine-tuned to optimize their catalytic properties. Thus, our findings pave the way for leveraging the full potential of these nanomaterials in catalysis.

Introduction

MXenes are 2D metal carbides or nitrides with the general formula $M_{n+1}X_n$, and they are formed by the stacking of one atom-thick layers of an early transition metal (M in the general formula) alternating with carbide or nitride sheets (X in the formula), with the total number of sheets being 3, 5 or 7.[1] The metal sheets in the MXene stack are always external and they are normally functionalized by surface terminal groups.

[a] Department of Organic Chemistry, Biochemistry and Catalysis, Faculty of Chemistry, University of Bucharest, Bdul Regina Elisabeta 4-12, Bucharest 030016, Romania. E-mail: vasile.parvulescu@chimie.unibuc.ro

[b] Instituto Universitario de Tecnología Química, Consejo Superior de Investigaciones Científicas-Universitat Politecnica de Valencia, Universitat Politecnica de Valencia, Av. De los Naranjos s/n, 46022 Valencia, Spain. E-mail: aprimoar@itq.upv.es

[c] Laboratory of Nanoscale Condensed Matter, The National Institute of Materials Physics, Atomistilor str. 405 A., Bucharest-Magurele, Romania

† Electronic supplementary information (ESI) available. See DOI: https://doi.org/10.1039/d5ey00004a

MXenes are obtained by Al etching of the M(Al)X phase, with the nature of the surface functional groups depending on the etching agents.[2]

Since their discovery in 2011 and due to their structure, electrical conductivity and electronic properties, these 2D materials have offered great potential in electrocatalysis, optoelectronics, renewable energy storage and biomedical applications.[3–5] As electrocatalysts, MXenes have shown excellent performance for the oxygen evolution (OER) and reduction (ORR) reactions, hydrogen evolution reaction (HER) and electrocatalytic CO$_2$ reduction (CO$_2$R) reaction, among other reactions.[6–8] The properties of a given MXene are modulated by the nature of the surface terminal groups that influence the electrical conductivity and electrocatalytic properties.[9]

Although early transition metals exhibit remarkable catalytic activity, the available reports on the activity of MXenes as thermal catalysts are currently limited to a few reactions, including the dehydrogenation of ethylbenzene and light alkanes, CO$_2$ hydrogenation, the water gas shift reaction and CO oxidation.[10–13] In these rare reports, MXenes often serve as passive supports to active metal

nanoparticles, metal clusters and even single atom sites,[14,15] rather than exhibiting intrinsic catalytic activity; therefore, the intrinsic active sites on MXenes still remain unexplored.

Considering the interest in exploiting the potential that the large family of MXenes (over 70 types already reported) could offer in heterogeneous thermal catalysis, due to the wide range of compositions and their tunable properties, it is somehow surprising that MXenes as thermal catalysts remain almost unexplored beyond a few (de)hydrogenation reactions.[16] The present study is aimed at filling this gap by providing new data on the catalytic activity of a Nb MXene as a heterogeneous catalyst for three general reactions in organic chemistry. Thus, herein we report the catalytic activity of Nb_2C MXene as: (i) bifunctional acid–base catalysts, (ii) oxidation catalysts to promote the oxidative coupling of aryl amines to aromatic azo/azoxy compounds, and (iii) catalysts for the selective hydrogenation of azoxybenzene to the corresponding azo compounds.

In the case of aldolic condensations, the reaction of aldehydes with carbonylic compounds are among the most common C–C bond forming reactions applied in organic synthesis due to the availability of the starting materials.[17] These reactions are catalyzed by homogeneous acids or bases. However, it was found that bifunctional acid–base solids having sites of weak or medium strength can be particularly suitable catalysts.[18] In the present study, it will be shown that the activity of Nb_2C MXene as a catalyst correlates with CO_2 and NH_3-thermoprogrammed desorption measurements, showing the simultaneous presence of basic and acid sites on Nb_2C MXene. The estimated TOF values rank Nb_2C MXene among the most efficient heterogeneous catalysts for these reactions, making them comparable, but better, than benchmark basic solids (such as MgO), solid acids (such as HZSM-5) and transition metal oxides.

Besides aldolic reactions leading to α,β-conjugated ketones, aromatic azo compounds are an important type of organic molecules used as dyes and pigments in the textile industry and as food additives.[19–21] Aromatic azo compounds are also the key components in many smart materials due to the reversible thermal and photochemical isomerization between the *E* and the *Z* stereo isomers, resulting in notable variations in the geometry and properties of both stereoisomers.[22,23] Oxidative coupling of aniline and substituted anilines has attracted considerable attention as an alternative to replace the use of stoichiometric oxo metal oxidizing reagents in the synthesis of azobenzenes.[24] The use of ambient oxygen and a catalyst to obtain azobenzenes represents a considerable advantage from the *green chemistry* point of view, since it does not generate wastes containing transition metals and the reaction exhibits a high atomic efficiency. Catalysts containing noble metals such as TiO_2-supported Au nanoparticles have been reported for this reaction,[25–27] but it would be more convenient to use noble metal-free catalysts. Herein, it will be shown that Nb_2C MXene is able to promote the aerobic oxidative coupling of anilines to a mixture of azo and azoxybenzenes, being possible to selectively hydrogenate the latter to obtain high azobenzene selectivity. DFT calculations shed light on the nature of the active sites of Nb_2C MXene that are responsible for the aryl aniline coupling, consisting of two neighboring free

Nb sites in order to promote coupling, and the reaction mechanism involving the nucleophilic attack of deprotonated aniline on the adsorbed Ph–N=O intermediate.

Experimental section

Synthesis of Nb_2C MXene

Nb_2C MXene was prepared by hydrothermal aluminum etching, starting from a commercial Nb_2AlC powder (Chemazone), as reported in the literature.[28] Briefly, 1 g Nb_2AlC was added to a solution of 1.5 g $NaBF_4$ and 30 mL of 37% HCl aqueous solution under magnetic stirring. The reaction mixture was sealed in a 100 mL Teflon-lined autoclave and kept for 8 h at 180 °C. After being cooled to room temperature, the resulting black suspension was filtered, and then washed several times with Milli-Q water until the suspension pH value was neutral. Finally, the obtained solid was dried at room temperature.

The resulting Nb_2C MXene clay was subsequently delaminated by ultrasound dispersion with a 700 W tip sonication system operating with 1 s on–off pulses for 5 h of a Nb_2C MXene clay sample previously expanded in DMSO for 24 h. Milli-Q water was used as a dispersing medium with the aim of achieving a Nb_2C MXene concentration of about 1 mg mL^{-1}. The Nb_2C MXene samples were recovered by centrifugation and resuspended in Milli-Q water three times to reduce the DMSO content of the sample that was used as the catalyst. A Nb_2C MXene sample underwent thermal activation at 350 °C under N_2 stream for 1 h in an oven to remove some surface functional groups and achieve an increase in the number of active sites.

Synthesis of MgAl-hydrotalcite

The hydrotalcite sample used as benchmark catalyst in the present study was obtained at a pH value of 10 under low supersaturation conditions by precipitating 250 mL of a solution of Mg and Al nitrate at a molar ratio of 3 and a total metal ion concentration of 1.5 M with a 250 mL basic solution obtained from 0.18 mol of Na_2CO_3 and 0.44 mol of NaOH in bi-distilled water. The synthesis was carried out at room temperature under vigorous stirring at 600 rpm. After completion of co-precipitation, the resulting gel was aged for 18 h at 75 °C, cooled to room temperature, then filtered and washed with bi-distilled water until a pH of 7 was achieved. The drying of the LDH gel was performed at 90 °C for 24 h under air flow. CO_2- and NH_3-TPD measurements indicate that the specific densities of the basic and acid sites in this sample based on the desorption at 120 °C are 0.1838 and 0.0271 mmol g^{-1}, respectively.

Characterization

Textural parameters of Nb_2C MXene were determined from N_2 adsorption–desorption isotherms at −196 °C using a Micromeritics ASAP 2010 Surface Area and Porosity Analyzer. H_2 pulsed chemisorption and H_2-TPD measurements were carried out in an AutoChem II 2920 station from Micromeritics. Before H_2 adsorption, fresh samples were heated at 450 °C (10 °C min^{-1}) under 30 mL min^{-1} He flow to desorb moisture and clean the

solid surface. Subsequently, the samples were cooled down to room temperature under constant He flow. Then, the pretreated samples were exposed to pulses of 5 vol% H_2 in He until the peak area corresponding to H_2 remained constant and no further H_2 uptake was detected. Subsequently, thermal H_2 desorption was carried out by heating the sample at a constant rate (10 °C min^{-1}) under He flow up to 450 °C. Acid–base properties of the investigated catalysts were titrated by NH_3- and CO_2-TPD measurements using the same Micromeritics instrument. Specimens were placed in a U-shaped quartz tube with 0.5 cm inner diameter and pretreated under He flow (Purity 5.0, from Linde) at 120 °C for 1 h. After this time, the MXene sample was exposed to a flow of CO_2 or NH_3 (from SIAD) for 1 h, and the samples were then purged at room temperature with a He stream (50 mL min^{-1}) for 20 min to remove any weakly adsorbed species. TPD measurements were subsequently performed at 10 °C min^{-1} heating rate up to 450 °C as the final temperature. The desorbed products were analyzed with a TC detector. The desorbed NH_3 or CO_2 amounts, expressed as mmols per gram of catalyst, were quantified using a calibration curve.

Powder X-ray diffraction (XRD) patterns in the 5–90° 2θ range were recorded on a Shimadzu XRD-7000 diffractometer using Cu K$_\alpha$ radiation (λ = 1.5418 Å, 40 kV, 40 mA) at a scanning rate of 2° min^{-1}.

Raman spectra were recorded in the frequency range from 150 to 4000 cm^{-1} at three different excitation wavelengths (325, 488 and 633 nm) using a Horiba Jobin Yvon LabRam high-resolution UV-Visible-NIR Raman spectrophotometer coupled with a Leica optical microscope.

Transmission electron microscopy (TEM) images of the Nb_2C MXene samples were acquired in a JEOL JEM 2100F under an accelerating voltage of 200 kV. Nb_2C MXene samples were prepared by depositing one microdrop of an aqueous suspension of the material immediately after sonication onto a carbon-coated holey nickel TEM sample holder. The water was spontaneously evaporated at room temperature before introducing the sample in the microscopy chamber. Atomic force microscopy (AFM) measurements of the exfoliated Nb_2C MXene particle thickness were carried out in the tapping mode in air at ambient temperature using a Veeco AFM apparatus. After exfoliation and sonication in water, one drop of the Nb_2C MXene sample suspensions was deposited on atomically flat mica plate and the water was allowed to evaporate under ambient conditions before measurements. Note that, in contrast to the subnanometric vertical resolution, the frontal views do not reflect the real lateral size of the platelets due to the width of the tip used in the measurements.

High-resolution X-ray photoelectron spectroscopy (XPS) analyses were performed with an AXIS Ultra DLD (Kratos Surface Analysis) instrument operating in ultra-high vacuum (10^{-9} mbar base pressure). The XPS instrument is equipped with a 165-mm hemispherical analyzer and a dual anode (Mg/Al K$_\alpha$) X-ray source. In this study, the monochromatic (Al K$_\alpha$, $h\nu$ = 1486.74 eV) X-rays produced by an X-ray gun operating at 144 W (12 kV × 12 mA) have been used for sample excitation. Sample charging effects were avoided using a flood gun (charge balance 2.7 V, filament current 1.5 A and filament bias 1 V). The acquisition setup has been operated in spectrum FOV2 mode using a pass energy filter of 40 eV with an analyzer aperture of 110 μm. Spectral analyses were carried out with the CASA program after baseline subtraction with the Shirley function.

Determination of the particle size of the Nb_2C MXene in the suspension and zeta potential measurements were carried out using Malvern Zetasizer instrument. Nb_2C MXene samples were well-dispersed *via* 5 min sonication in aqueous solution at neutral pH prior to the measurements.

Catalytic tests

All substrates and reagents were purchased from Sigma-Aldrich, and used without any further purification. The following formulae were used to determine the substrate conversion, product selectivity and turnover frequency values (TOFs):

$$\text{Conversion (\%)} = \frac{(m_0 - m_t)}{m_0} \times 100$$

$$\text{Selectivity (\%)} = \frac{m_p}{m_0 - m_t} \times 100$$

$$\text{TOF } (h^{-1}) = \frac{m_0 - m_t}{n_{AS} \times \text{time}}$$

In the above mentioned equations, m_0, m_t, m_p and n_{AS} correspond to the initial substrate moles, substrate moles at a given time, product moles and number of active sites in moles on the catalyst. Unless otherwise stated, the reactions were carried out in triplicate, and the values of the conversion and selectivity correspond to the average value of the measurements.

Cyclohexanone condensation

Aldol condensation of cyclohexanone and benzaldehyde or furfural was carried out under solvent-free conditions or with heptane as the solvent by reacting a mixture of 1 mmol cyclohexanone with benzaldehyde (2 mmol, 120 °C) or furfural (5 mmol, 90 °C), and in the presence of 20 mg catalyst (cyclohexanone/catalyst wt ratio of 5) in a round-bottom flask under 500 rpm of magnetic stirring for 2 h. At the end of the reaction, the catalyst was removed from the mixture by filtration, and the liquid phase analyzed by ^{1}H NMR spectroscopy and GC-FID chromatography. ^{1}H NMR spectra were recorded in CDCl$_3$ as solvent on a Bruker Avance III Ultrashield Plus 500 MHz spectrometer, operating at 11.74 T, corresponding to the resonance frequency of 500.13 MHz for the ^{1}H nucleus. The GC-FID chromatograph was equipped with a 30 m length 0.25 mm capillary column with DB5 stationary phase. The reaction compounds were identified by mass spectrometer-coupled chromatography, using a GC/MS/MS Varian Saturn 2100 T equipped with a CP-SIL 8 CB Low Bleed/MS column of 30 m length and 0.25 mm diameter.

Procedure for the oxidative coupling of aniline to azobenzene and azoxybenzene

Direct coupling of aniline to a mixture of azobenzene and azoxybenzene was performed under autogenic pressure. A

mixture of aniline (1 mmol), Nb_2C MXene catalyst (50 mg) and toluene (2 mL) was added into a 7 mL stainless steel autoclave. The reaction mixture was heated at a temperature of 80 °C or 150 °C under continuous magnetic stirring (800 rpm). The reaction time was 24 h or 48 h. After the required time, the autoclave was cooled to room temperature, the catalyst was recovered by centrifugation, and the reaction products were analyzed. Alternatively, the autoclave can be purged with Ar for 15 min, then charged with H_2 at 5 bar, and the system can be heated again at 150 °C for 14 h under magnetic stirring to reduce the azoxybenzene present in the reaction mixture into azobenzene. The reaction products were analyzed by a CG-MS apparatus (Thermo Scientific Trace 1310 chromatograph coupled with a ISQ LT mass spectrometer as detector) equipped with a non-polar GC separation column (TG-5SilMS, 30 m × 0.25 mm × 0.25 μm) operated with He as the carrier gas. The temperature program of the chromatography was set to 45 °C for a dwell time of 6 min. Afterwards, the temperature was increased at a rate of $10\,°C \times min^{-1}$ up to 240 °C, maintaining this final temperature for a dwell time of 10 min. Mass spectra were recorded in a positive polarization mode in the range of m/z 50–300 atomic mass units.

Results

Nb_2C MXene was obtained from commercial Nb_2AlC by Al etching with *in situ* generated HF formed *via* the reaction of $NaBF_4$ with concentrated HCl, followed by exfoliation of the resulting accordion-like MXene clay by expansion with DMSO for the first 24 h and subsequent ultrasound treatment. BET and Langmuir specific surface area values of the Nb_2C MXene powders were very small, 2.5 and 2.7 $m^2\,g^{-1}$, respectively. The small difference between the BET and Langmuir area values confirms the absence of micropores. This small surface area of MXene as powders is known,[28] as the sheets tend to stack and these solids do not have permanent porosity. A specific surface area of Nb_2C MXene of 1.68 $m^2\,g^{-1}$ has been previously reported for exfoliated Nb_2C MXene powders.[29] However, it should be noted that in a suspension with efficient sonication, easily dispersible Nb_2C MXene samples should have a much larger surface area due to deaggregation and partial exfoliation of the particles dispersed in the liquid medium. Indirect surface area measurement in aqueous suspension by the methylene blue association titration method[30] may show values as high as 161 $m^2\,g^{-1}$ for Nb_2C MXene samples.[31] In the present case, a specific surface area of 55 $m^2\,g^{-1}$ was estimated for Nb_2C MXene aqueous suspensions using the methylene blue method (see Fig. S1 in ESI†).[31] Methylene blue is a cationic dye that strongly associates with negatively charged particles, like MXenes, forming a single coverage layer as determined by optical spectroscopy that can be distinguished by the absorption maximum wavelength and spectra of methylene blue in solution, solid and in its dimeric forms. Thus, the surface area is determined from the titration point, in which all methylene blue is associated to the MXene.[31] Dynamic laser scattering indicates the presence of particles in these aqueous suspensions (see Fig. 1) with a broad distribution from 200 to 600 nm, where the most abundant particles are about 300 nm in suspension. Zeta potential measurements indicate that these Nb_2C MXene particles bear a negative charge with a zeta potential value of −35 mV at neutral pH (Fig. 1), corresponding
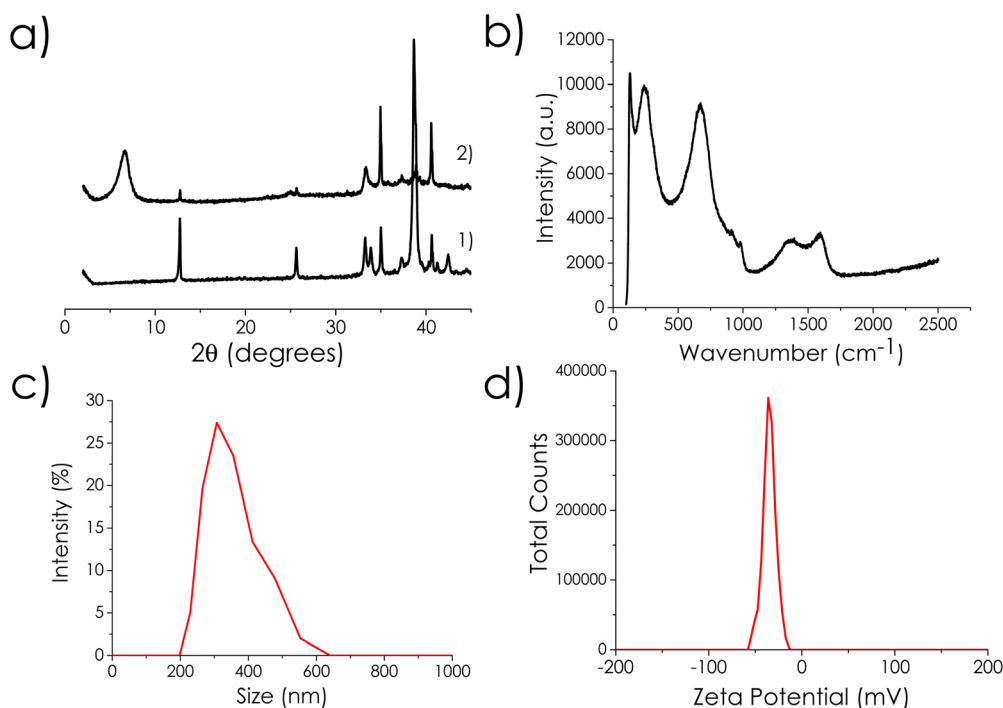
Fig. 1 (a) XRD spectra of Nb_2AlC (1) and Nb_2C MXene (2) after Al etching. (b) Raman spectrum of Nb_2C MXene recorded with a 413 nm excitation. (c) Dynamic laser scattering of aqueous suspensions of Nb_2C MXene (1 mg mL^{-1}). (d) Zeta potential of aqueous Nb_2C MXene suspension at neutral pH.

to indefinitely persistent colloidal dispersions. It should be noted, however, that the reactions under study will be carried out in hydrocarbons.

Table 1 presents the results of H_2 pulsed chemisorption and H_2-, CO_2- and NH_3-thermal desorption (TPD) measurements. These techniques indicate little agreement between the chemisorbed and desorbed hydrogen. Molecular hydrogen can interact with MXenes via physisorption, Kubas-type interaction with the transition metal and chemisorption by H_2 dissociation into H atoms.[32] These different interactions can explain the higher value of H_2 chemisorption in comparison to H_2-TPD. Previously, the presence of two broad peaks at 140 and 352 °C in H_2-TPD of 2D Mo_2C has been observed, and attributed to the presence of two different H_2 chemisorption sites.[33] A similar interpretation can be done here for the 166 and 392 °C peaks in H_2-TPD of 2D Nb_2C MXene. Both the acid and basic sites of this material were rather small, considering the low amount of chemisorbed NH_3 and CO_2 molecules (0.03 mmol g^{-1} or lower chemisorbed probe, Table 1). In general, the low acidity–basicity values are in agreement with the small surface area of these Nb_2C MXene samples as powders. The range of desorption temperatures for NH_3 and CO_2 (between 300 and 400 °C) indicates that the Nb_2C MXene sites have a strength between weak and medium. A strong interaction of NH_3 with MXenes (chemisorption) has been reported to appear only on the O-terminated MXenes, and this interaction can be altered depending on the surface terminal groups.[32] Therefore, acid sites could be Nb–O–H hydroxyls or surface termination vacancies leaving under coordinated Nb atoms, while basic sites would be some surface O atoms having negative charge or high electronic density. Furthermore, in the present case, it is proposed that the sites that interact with NH_3 correspond to the surface group vacancies, therefore measuring the accessible metal sites. It is expected that a portion of the stronger active sites that chemisorb NH_3 will be those that can interact with aromatic amines promoting the oxidative coupling. Therefore, it is proposed that the amount of adsorbed NH_3 corresponds to the maximum possible sites available to aniline activation, which should be a fraction of them. The low NH_3 desorption values would thus indicate a low density of surface vacancies and defects.

It may be possible that suspending Nb_2C MXene in a solvent could make a few more centers available, as a consequence of

the higher layer expansion and larger accessibility of the sites. Therefore, although the structure of the active site on Nb_2C MXene and the exact nature of defects can be quite complex, these desorption measurements provide a useful, initial quantitative information on the number and strength of the acidic and basic sites on Nb_2C MXene, which can be correlated later with its catalytic activity.

ICP-OES chemical analysis of the Nb_2C MXene sample under investigation indicates that the residual Al content is 1.41%, while it is 17.96% for the Nb_2AlC precursor. This indicates that the percentage of Al containing impurities, which is mainly attributable to Al_2O_3, is low and similar to those amounts that have been reported in the literature.[28] The experimental Nb content for Nb_2AlC and Nb_2C MXene is 39.95% and 52.11%, respectively. Although the percentage of Nb increases from Nb_2AlC to Nb_2C MXene, it is still lower than expected for the Nb_2C MXene formula, indicating a significant contribution of the sample of the terminal functional groups, F and oxygenated functions, and the exfoliating agent DMSO to the elemental composition. With the experimental Nb content and considering the presence of DMSO, a possible formula of the samples used in the catalytic study would be $Nb_2C(F,O)_2 \cdot 1.5DMSO$. The presence of DMSO was detected by solid state ^{13}C NMR spectroscopy in the sample used for the present study.

XRD shows that the pattern of the Nb_2AlC phase (PDF 00-030-0033) diminishes considerably upon Al etching, rendering Nb_2C MXene. In particular, the (002) line at 13° of the Nb_2AlC precursor exhibits residual intensity after Al etching treatment, while a new broad (002) diffraction band appearing at a much shorter diffraction angle of about 6° is recorded. This broad peak corresponds to the accordion-form of the Nb_2C MXene material, and indicates the considerably expansion of the interlayer distance to 1.47 nm upon Al etching. In precedent studies in the literature, it has been found that this large Nb_2C MXene interlayer distance corresponds to situations in which the intercalating agent (DMSO in the present case) is still incorporated in the material.[34] Other XRD lines corresponding to Nb_2C MXene (PDF 01-077-9683) appearing at 2θ values of 40.32°, 58.34°, and 73.31° that can be indexed to the (200), (220), and (222) facets (Fig. 1), respectively, were in agreement with the literature.[35]

The Raman spectra of Nb_2C MXene upon 413 nm laser excitation showed peaks at 235 and 664 cm^{-1}, accompanied by a shoulder at 957 cm^{-1} (Fig. 1b).[36,37] These three peaks are ascribed to the vibrations of Nb^{III}. Thus, the bands at about 235 and 664 cm^{-1} correspond to E_{2g} (in-plane vibrations of Nb–C atoms and surface groups attached to Nb) and A_{1g} (out of plane vibrations of C atoms in Nb–C bonds) modes, respectively.[38,39] On the other hand, peaks at 1380 and 1580 cm^{-1} are attributable to the D and G bands, respectively, of the carbide layer.[36]

The XPS analysis of the Nb_2C MXene samples under study shows that this material contains C, Nb, F, S and O. XPS allowed for determining the relative atomic ratio of F and O with respect to Nb, corresponding to the formula $Nb_2CF_{0.12}O_{0.56}$. This means that the sample has a defective number of surface functional groups. Depth profiling using fast

Table 1 Pulsed H_2 sorption and H_2-, CO_2- and NH_3-TPD measurements for Nb_2C MXene

Experiment	Temperature (°C)	Gas uptake/desorption (mmol g^{-1})
Pulsed H_2 sorption	RT	2.12
H_2-TPD	166	0.52
	392	1.04
	Total	1.56[a]
CO_2-TPD	318	0.03
NH_3-TPD	316	0.01

[a] The difference between the amounts of H_2 sorption and total H_2 desorption corresponds to the weakly physisorbed H_2 molecules.

Ar bombardment for 10 min shows a considerable decrease in the atomic percentages of F and O, meaning that these groups are mainly located on the external surface. Fig. 2 shows the experimental spectra of each element, together with the best deconvolution to individual components having various oxidation states or coordination sphere. The exact binding energy and contribution to the total signal of each component is also indicated in Fig. 2. Thus, as shown, the C1s spectrum can be deconvoluted into four components, corresponding to a major contribution of C atoms bonded to Nb (282.8 eV), two other contributions corresponding to the typical C sp^2 atoms (284.5 eV) and two C families bonded to OH (286.5 eV) and C=O (288.3 eV). In the case of the Nb 3d core level, the two expected peaks of Nb $3d_{5/2}$ and Nb $3d_{3/2}$ that occur due to spin–orbit coupling were recorded. Deconvolution of each peak shows contributions corresponding to Nb having Nb^{III} and Nb^{II} oxidation states, accompanied by another component corresponding to Nb bonded to C. Regarding the surface terminal groups, the peaks corresponding to F 1s and O 1s were recorded. In the case of the F 1s peak (684.7 eV), there is a single component attributable to F atoms bonded to Nb. For the O 1s spectrum, three different environments appearing at 528.2, 529.5 and 530.8 eV can be ascribed to O atoms bonded to Nb^{II}, Nb^{V} and adsorbed H_2O, respectively. XPS deconvolution and the interpretation both agree well with previous reports in the literature.[40,41]

In comparison with Nb_2AlC, the Nb content determined using XPS increases from 39.95% to 52.11% upon Al etching and formation of Nb_2C MXene. The increase of the Nb percentage is a consequence of the removal of Al. Also, the Nb/C atomic ratio estimated for Nb_2C MXene using XPS was 0.69, while that of the Nb/O ratio was 0.43. The surface atomic O/C ratio was 1.6. These atomic ratios indicate a defective amount of Nb with respect to C and O, according to the ideal M_2CT stoichiometry, in which M stands for Nb and T corresponds to O. This discrepancy would indicate again the presence of some DMSO intercalating agent adsorbed on the MXene surface, which is in line with the ICP analysis and the expanded interlayer spacing determined by XRD.

The high crystallinity of the Nb_2C MXene particles was definitely confirmed by TEM images, showing the characteristic 2D morphology expected for a MXene sample with sheets of lateral dimensions larger than 1 μm, accompanied with some smaller sheets of hundreds of nm. Fig. 3 shows some selected images at various magnifications. Fig. 3 also presents a high-resolution TEM image visualizing the crystallinity of the Nb_2C MXene material with interatomic fringes of 0.228 ± 0.001 nm, which is close to the value of 0.23 nm that has been previously reported.[42] Selected area electron diffraction also confirms the crystallinity of the Nb_2C MXene sheets. Overall, these data are in agreement with the characterization reported in the literature.[35]

The thickness of the Nb_2C sheets was determined by AFM measurements. Fig. 4 shows a frontal view of Nb_2C MXene taken by AFM on atomically flat mica substrate, as well as some vertical profiles along certain lines that are used to determine
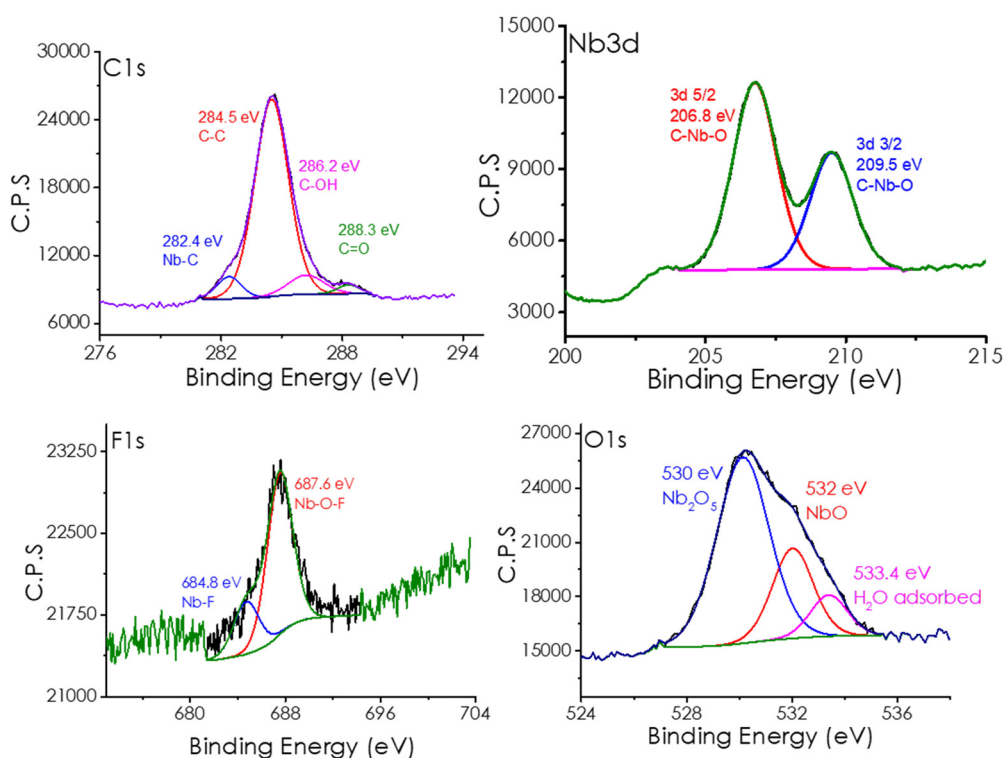

Fig. 2 High-resolution XPS peaks of the elements detected in Nb_2C MXene, showing the best deconvolution for each spectrum into the individual components whose assignment, binding energy and contribution percentage are indicated in the plot.
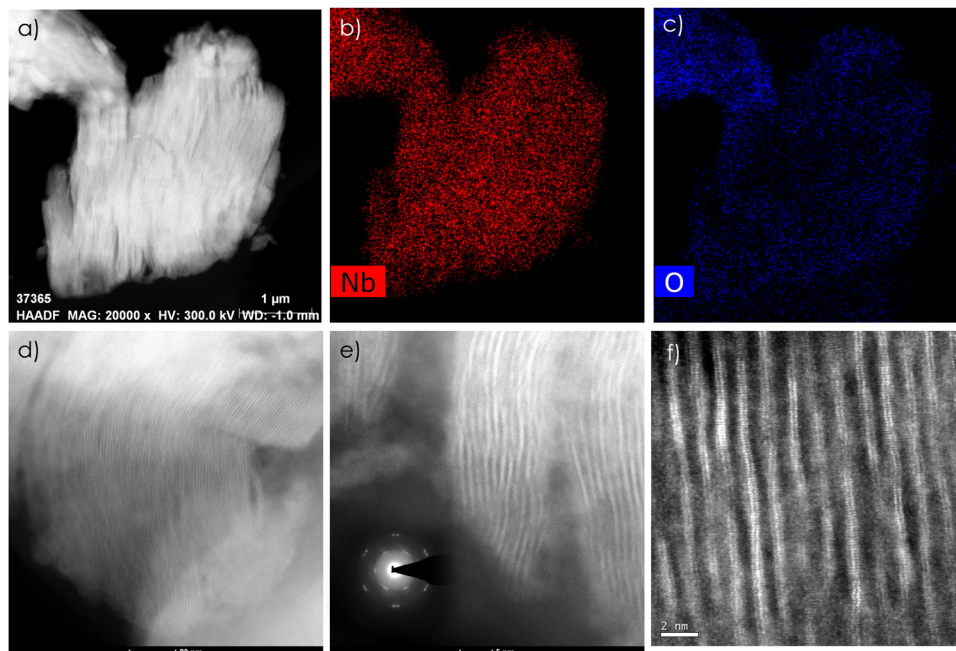
Fig. 3 TEM images of the Nb_2C MXene sample under study, showing the 2D morphology at four magnifications (a), (d), (e) and (f), and the Nb (b) and O (c) distribution mappings of Fig. 3a. The inset of Fig. 3e shows high crystallinity of the Nb_2C sheets.

the thickness of the Nb_2C sheets. These measurements indicate that most of the sheets have a thickness of about 1.5 nm after sonication, which is the reported thickness for the Nb_2C monolayer obtained from Nb_2AlC etched by SnF_2 molten salt and subsequent NaOH treatment of the Nb_2C clay to achieve water dispersibility and exfoliation.[35] Therefore, most of the dispersed Nb_2C MXene material should correspond to a single layer or a few layers MXene. The crystallinity and lattice fringe measurement of the Nb_2C sheets under study are shown in Fig. 5.

In an attempt to associate the acidic and basic sites to structural defects, EPR of Nb_2C MXene was measured without observing the presence of any signal, meaning that the Nb_2C MXene sample does not have unpaired electrons. Also, HAADF-STEM images with atomic resolution were recorded, showing a high degree of crystallinity (Fig. 5). These images do not easily

detect light elements like C, O and F. However, XPS depth profiling using Ar^+ sputtering indicates an O/Nb atomic ratio on the surface of 2.32 that decreases as the innermost layers of the material is probed.

Catalytic behavior

Aldol condensation. As commented earlier, NH_3 and CO_2-TPD measurements indicate that Nb_2C MXene has some acidic and basic sites of weak and moderate strength. This density of sites is between 3 and 10 times lower than typical porous materials used as solid acids or bases, which can also exhibit higher strength.[43] However, it has been found that bifunctionality, *i.e.*, the simultaneous presence of both acidic and basic sites often of weak or moderate strength in a solid with spatial proximity, can be favorable from the catalytic point of view for
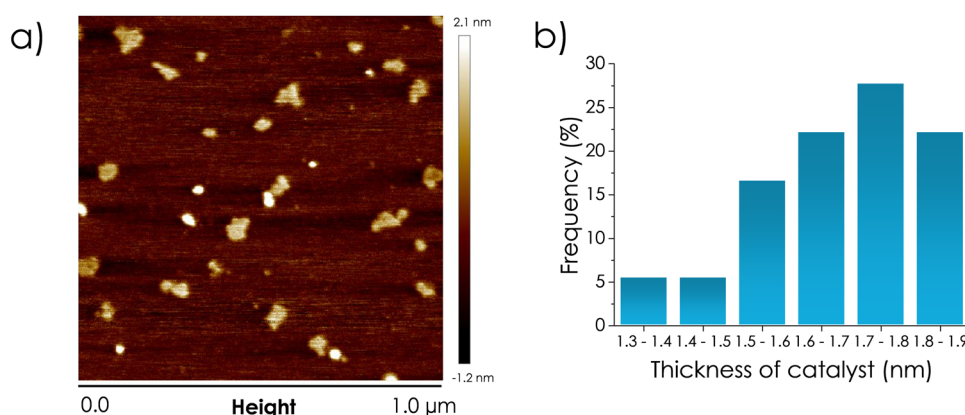

Fig. 4 (a) Frontal view of the Nb_2C MXene sample on an atomically flat mica. (b) Vertical profiles along ten different particles, showing a modal thickness value in the range 1.7–18 nm.
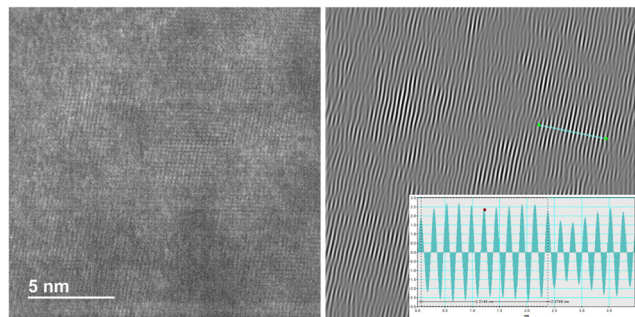
© 2025 The Author(s). Published by the Royal Society of Chemistry

Fig. 5 HAADF-STEM images of Nb_2C MXene, in which the presence of Nb defects has been highlighted by arrows. The insert shows the periodic regular fringes along the white line in the right image indicating a high crystallinity.

certain reactions.[44] This is the case for aldolic condensations, in which bifunctionality can serve to simultaneously activate the two reagents, *i.e.*, acidic sites activate the aldehyde, while basic sites activate the α position of the carbonylic compound.[18]

Aldolic condensation of aldehydes and ketones is a reaction type that is widely used in organic synthesis for the preparation of complex molecules by forming C–C bonds at the α position of the easily available carbonylic precursors.[45] While strong acids or bases, such as $AlCl_3$ or KOH, are frequently used to promote aldolic condensations in the homogeneous phase, the reaction can occur even if the strength of the sites is considerably weaker when the two types of sites are simultaneously present on a bifunctional solid.[18] This has been observed in ALPONs and other solids.[18]

In the present study, we first studied the aldolic condensation of cyclohexanone with benzaldehyde (Scheme 1). A blank control in the absence of any catalyst under the reaction conditions showed that condensation of benzaldehyde and cyclohexanone occurs to a low extent (Table 2). The presence of Nb_2C MXene significantly increases product formation, resulting in a mixture of mono- and di-condensation products with excellent carbon balances, higher than 90%. According to isothermal N_2 gas adsorption measurements on dry samples, it should be noted that although the Nb_2C MXene as a powder has a small surface area of *ca.* 2.5 m^2 g^{-1}, the surface area of these dispersed 2D sheets can be remarkably higher when suspended on a liquid medium.[31] This is because suspension in a liquid medium makes it possible to have dispersed, exfoliated MXene platelets with much less stacking in the solvent. However, they collapse and aggregate when the sample is dried. Comparison with MgO and hydrotalcite, as benchmark basic solids having strong or medium basic strength sites, indicates that the cyclohexanone conversion

and turnover frequency values (TOFs) are higher for Nb_2C MXene. The cyclohexanone conversion and TOF values are also higher for Nb_2C MXene in comparison to HZSM-5, taken as a reference acid catalyst with strong acid centers, showing the superiority of Nb_2C MXene for this reaction due to its bifunctionality. In an attempt to further increase the density of the active sites, Nb_2C MXene was submitted to thermal activation at 350 °C under an inert atmosphere to remove some surface functional groups. However, the resulting Nb_2C MXene sample was less active than without this thermal treatment. This is probably due to the surface restructuration and healing of structural defects, rather than the increase in these sites.

Stability of the Nb_2C MXene as a catalyst was confirmed by performing five consecutive uses of the same Nb_2C MXene sample under incomplete cyclohexanone conversion, conditions that ensure that a decrease in catalyst activity could be observed. Fig. 6 shows the conversion and selectivity to mono- and di-condensation product at 2 h reaction time. As shown, a slight decrease in cyclohexanone conversion from 51% to 46% was observed after five consecutive uses, but this minor decrease could be due to the imperfect recovery of the Nb_2C MXene sample from one run to another. Also, a small variation of selectivity for the di-benzylidene adduct from 54% to 51% was noted. In addition, chemical analyses of liquid solutions after the reaction indicates that the Nb content was below 10 μg L^{-1}, corresponding to a maximum leaching of 0.5% of the initial Nb content of the Nb_2C MXene catalyst. Meanwhile, TEM and XPS show that Nb_2C MXene remains crystalline and without significant changes after five consecutive uses.

Cyclohexanone also reacts with furfural in the presence of Nb_2C Mxene as a bifunctional acid–base catalyst (Scheme 2). The conversion rate of cyclohexanone in the reaction with furfural reached 26% at 2 h, while the selectivity was completely directed to the mono-condensation product ((2E)-2-[2-furylmethylene]cyclohexanone). The calculated TOF value for Nb_2C Mxene was 152 h^{-1} based on the density of basic sites, confirming the high activity of this catalyst. When using NaOH as a homogeneous basic catalyst, the reaction does not stop at the mono-condensate product, resulting in the formation of the di-condensate one.[46]

The scope of the reaction was further extended to the reaction of cyclohexanone with saturated aliphatic aldehydes, like acetaldehyde and isobutyraldehyde. Comparison with hydrotalcite again shows a better performance of Nb_2C Mxene. Nb_2C Mxene also promotes the condensation of cyclohexanone with conjugated aldehydes, like 2-butenal and cinnamaldehyde, although with much lower TOF values, as expected in view of the electronic effects on the aldehyde group. In the case
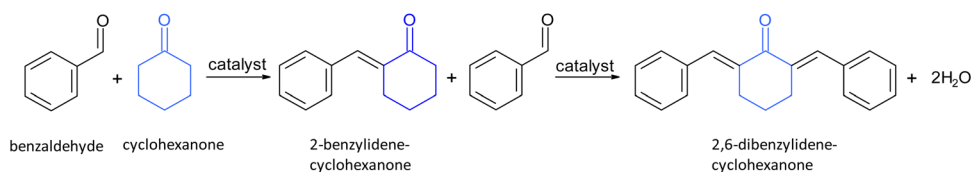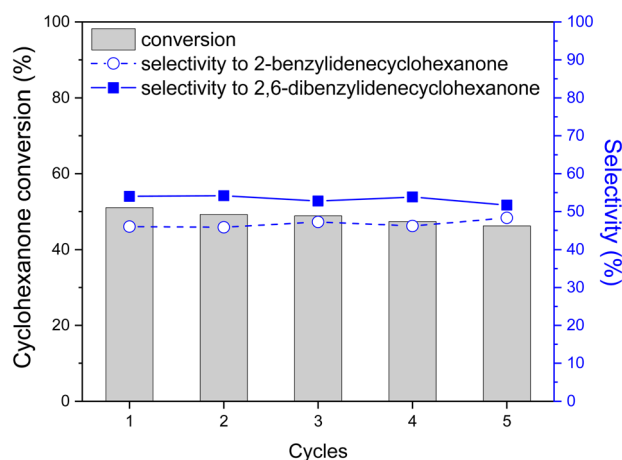

Scheme 1 Aldolic condensation of cyclohexanone and benzaldehyde.

Table 2 Aldol condensation of cyclohexanone with benzaldehyde under solventless conditions

Catalysts	Cyclohexanone conversion[a] (%)	TOF[b] (h^{-1})	Selectivity (%)	
			2-Benzylidene-cyclohexanone	2,6-Dibenzylidene-cyclohexanone
Blank[c]	16 ± 2	—	5	95
Blank	< 5	—	100	—
Nb$_2$C	51 ± 5	855	46	54
Nb$_2$C[d]	22 ± 2	366	24	76
MgO	31 ± 3	25	3	97
HT[e] Mg/Al = 3	56 ± 5	77	2.81	97.19
HZSM-5[c]	24 ± 3	654	8	92

Reaction conditions: Temperature 120 °C, time 2 h. [a] Standard deviation based on three independent measurements. [b] Calculated with respect to the density of basic sites determined by CO$_2$-TPD. [c] Presence of benzoic acid. [d] Heptane (2 mL) as the solvent. [e] HT corresponds to hydrotalcite.

Fig. 6 Catalytic activity of the Nb$_2$C MXene sample after 5 cycles in the condensation of cyclohexanone with benzaldehyde. Reaction conditions: cyclohexanone 1 mmol, benzaldehyde 2 mmol, catalysts 20 mg, no solvent, reaction temperature 120 °C, magnetic stirring at 500 rpm, and time 2 h.
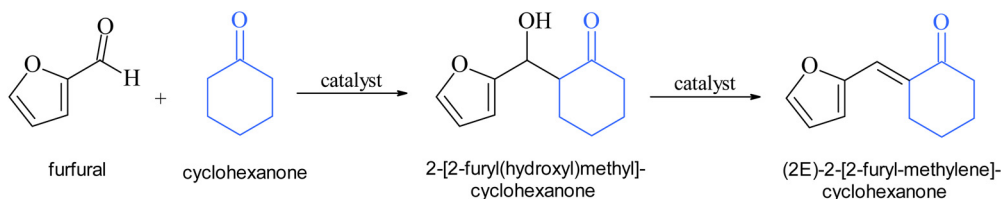
of propenal, Michael addition of the enolate to the conjugated C=C double bond was observed, but a higher temperature was necessary to achieve better conversion (see footnote b in Table 3). Nb$_2$C Mxene is even able to promote the self-condensation of ketones, such as cyclohexanone to 2-cyclohexylidene cyclohexanone, but it failed for the condensation of salicylaldehyde and p-(dimethylamino)benzaldehyde. Table 3 summarizes the results of the substrate scope screening. Worth noting is that while selectivity respect to cyclohexanone

conversion to the condensation products is complete, product selectivity respect to aldehyde can be much lower. This is because an excess of aldehyde is used in the reaction and aldehyde oxidation or self-condensation can be formed in some extent. Particularly, in the case of propanal, the self-condensation to 2-methyl-2-pentenal was the only product observed in high yield. Overall, Table 3 shows the general scope of Nb$_2$C as an acid/base catalyst to promote aldolic condensations.

The previous results show the high activity of Nb$_2$C Mxene in comparison with other acidic (HZSM-5) and basic (MgO, hydrotalcite and NaOH) catalysts. This higher activity is remarkable, considering the low density of the acidic and basic sites measured by NH$_3$ and CO$_2$ thermodesorption, and also their weak/medium strength. We propose that this high activity arises from the bifunctional acid–base nature of Nb$_2$C Mxene and their appropriate strength. These acid–base strengths of the sites should depend on the work function and other collective properties of the Nb$_2$C Mxene, since they determine the electronic density of the active sites, and therefore the acidity and basicity.

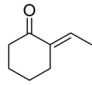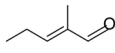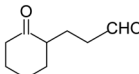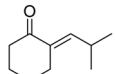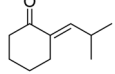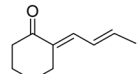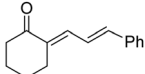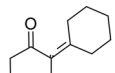**Oxidation of anilines to aromatic azo and azoxy compounds.** Oxidative coupling of aniline to azo- and azoxy-benzenes is a reaction that can typically be catalyzed by metallic nanoparticles or metal oxides using molecular oxygen or hydrogen peroxide as terminal oxidizing reagents (Scheme 3).[24,25,47] Blank controls that were carried out in this study under the reaction conditions, but in the absence of any catalyst, indicated no detectable formation of azobenzene or azoxybenzene. In the presence of Nb$_2$C Mxene as the catalyst, analysis of the reaction mixture indicated the formation of both azo and azoxy compounds with a carbon balance higher than 95% (Scheme 3). The increase of the temperature from 80 °C to 140 °C or reaction time from 24 h to 48 h was accompanied by an increase of aniline conversion. The ratio between the azo and azoxy products depends on the reaction conditions (Table 4). Comparison of the azo-/azoxybenzene selectivity at very similar conversion shows that an increase in temperature from 80 °C to 140 °C favors azoxybenzene (entries 2 and 3 of Table 4). The same Nb$_2$C Mxene sample was used in a consecutive run, observing very minor decay in activity. Structural stability of Nb$_2$C Mxene was confirmed by characterization of the catalyst after the reaction, observing that the 2D morphology, XRD, Raman and XP spectra remained unaltered in the catalytic process. Stability of the catalyst surface was also confirmed using XPS analysis (Fig. S2, ESI†), which showed that the used Nb$_2$C Mxene material retained the XPS Nb 3d core level with the

Scheme 2 Condensation of cyclohexanone and 2-furfural.

furfural + cyclohexanone —catalyst→ 2-[2-furyl(hydroxyl)methyl]-cyclohexanone —catalyst→ (2E)-2-[2-furyl-methylene]-cyclohexanone

Table 3 Scope of Nb_2C Mxene as the catalyst promoting the aldolic condensation of cyclohexanone with other carbonylic compounds. Reaction conditions: cyclohexanone 1 mmol, carbonylic compound 2 mmol, catalyst 20 mg, solventless conditions, temperature 120 °C except indicated, time 2 h

Carbonylic compounds/ catalyst	Conversion (%)	TOF (h^{-1})	Product (selectivity with respect to cyclohexanone)	Remarks
Acetaldehyde Nb_2C/ Mxene	9	139	(38)	Acetic acid and cyclohexanone self-condensation are also observed as the product
Propanal/Nb_2C Mxene	84[a]	1405	(93)	No reaction with cyclohexanone
Propenal[b]/Nb_2C Mxene	12	198	(58)	Conjugate Michael addition
Isobutylaldehyde/Nb_2C Mxene	74	1240	(100)	Isobutyric acid is also formed in the presence of oxygen
Isobutylaldehyde/HT Mg/ Al = 3	55	296	(100)	
2-Butenal/Nb_2C Mxene	2	33	(100)	Octatrienal is also detected in the reaction mixture
Cinnamaldehyde	2	33	(100)	Cinnamic acid was also formed in the presence of oxygen
Cyclohexanone	2.5	50	(100)	
4-$(Me_2N)C_6H_4CHO$	0	0	—	No condensation products are observed

[a] The value refers to propanal conversion. [b] Temperature 150 °C.

expected $3d_{5/2}$ and $3d_{3/2}$ due to spin–orbit coupling. Meanwhile, the O 1s showed an increase in the proportion of the NbO component at 532 eV $vs.$ the Nb_2O_5 observed at 530 eV. This stability confirmed by XRD and XPS contradicts a generalization of the poor Mxene stability under aerobic conditions in aqueous solvents.[48,49] However, it has been observed that the

stability of Mxenes can be much better in organic solvents, as is the present case.[49]

Selectivity towards the most wanted azobenzene could be increased by subsequent reduction of azoxybenzene to azobenzene. This would require a treatment of the azo- and azoxybenzene mixture resulting from the oxidative aniline coupling with a reductive atmosphere in the presence of an efficient reduction catalyst.[40–43] To check this possibility and to know if Nb_2C Mxene is also able to catalyze the reduction step, air was replaced by hydrogen after an initial aniline oxidation, and the mixture was allowed to continue reacting in the presence of Nb_2C Mxene. The results are also presented in Table 4, showing that this two step-one pot process leads to an obvious enhancement of the azobenzene selectivity that can reach up to 98% (entry 4 in Table 4).
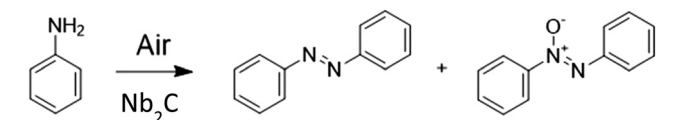
Scheme 3 Oxidative coupling of aniline to azobenzene and azoxybenzene.

Table 4 Results of the catalytic oxidative coupling of aniline to azo- and azoxy-benzene using air as an oxidant, and after treating the reaction mixture in the same pot with a subsequent reduction step with hydrogen

			Atmosphere				
			Air (5 atm)			Hydrogen (5 atm)	
				Selectivity (%)		Selectivity[b] (%)	
Run	Temp (°C)	Time (h)	Conversion[a] (%)	Azobenzene	Azoxybenzene	Azobenzene	Azoxybenzene
1	80	24	4.5	69.8	30.2	88.4	11.6
2	140	24	7.4	76.6	23.4	93.4	7.6
3	80	48	7.2	64.3	35.7	92.8	7.2
4	140	48	11.6	61.5	38.5	98.4	1.6
5[c]	140	48	9.8	64.5	35.5	93.0	7.0

Reaction conditions: 1 mmol aniline, 10 mL toluene, 10 mg Nb_2C MXene catalyst. [a] Conversion of aniline. [b] Selectivity after treating the initial azobenzene/azoxybenzene mixture of oxidation with a second hydrogenation step in the same pot using H_2 at the indicated temperature for 10 h. [c] Two times used Nb_2C MXene sample.

Computational calculations of the reaction mechanism. Computational calculations have been carried out *via* both CASTEP DFT code and Matlantis neural network potential, the details of which can be found in the ESI.† The model consisted of a geometry-optimized cell of 36 Nb_2CO_2 units, in which two O atoms were removed, resulting in a total of 178 atoms. Along the [001] direction, the thickness of the MXene is 4.7 Å, adding a sufficient vacuum space to ensure the absence of interactions in the periodic boundary calculations. A full reaction coordinate comprising all the reaction intermediates has been explored *via* a synergetic CASTEP-Matlantis evaluation, using both methods to find the true minima of all considered reaction intermediates. The proposed reaction mechanism and energy profiles are shown in Fig. 7.

The reaction mechanism involves adsorption of aniline on a position with two O defects on the Nb_2CO_2 MXene surface in close proximity. Initial calculations with models of Nb_2CO_2, in which the surface contained the stoichiometric O functional groups or a single O vacancy, did not result in any reasonable reaction mechanism. This double O vacancy defect is capable of adsorbing aniline on one defect, in which the surface is able to abstract a hydrogen atom from aniline (intermediate 3), generating a OH termination in a slightly endothermic step. The following step involves the highly exothermic chemisorption of O_2 on the other free O vacancy. This step adsorbs the molecule through one O atom, while the other O atom becomes activated for the coupling reaction with the deprotonated aniline. The activated O generates the Ph-NHO intermediate (step 5). This intermediate undergoes a hydrogen transfer to the MXene surface, generating intermediate 6 with a new OH termination and nitrosobenzene, which remains tightly bound to the O-vacancy.

The two formed OH terminations condense under the reaction conditions, generating a water molecule, thus regenerating one O-vacancy in an endothermic step. This could explain in part the enhanced conversion rates observed when increasing the reaction temperature. These conditions could desorb H_2O, increasing the number of O-vacancy sites, thus increasing the active sites for catalysis.

Intermediate 7 is generated when both nitrosobenzene and O-vacancy are formed. The next step (step 8) involves the displacement of the adsorbed H_2O molecule by another aniline molecule, which binds to the O-vacancy position in close proximity to the nitrosobenzene intermediate. The partial occupancy of the O-vacancy, sterically hindering aniline adsorption, results in lower adsorption energy with respect to the first aniline adsorption (-2.20 *vs.* -0.82 eV in Matlantis). After adsorption, the next intermediate (step 9) is formed with another hydrogen transfer from the second aniline to the MXene surface. This deprotonated aniline is nucleophilic enough to couple with the adsorbed nitrosobenzene moiety, in an exothermic step that completely breaks the N–O bond. This oxygen atom populates one full O-vacancy, while the newly formed 1,2-diphenyl-1λ^4-diazene (Ph-NHN-Ph) adduct (step 10) remains adsorbed to the other O-vacancy.

In order to generate the azobenzene product, the remaining N–H hydrogen in the molecule is transferred to an O-termination on the surface, yielding intermediate 11 in an endothermic process. The last step involves desorption of azobenzene from the O-vacancy and regeneration of the other O-vacancy *via* water formation, in the same way as described in step 7. This step from intermediate 11 to 12 should correspond to the rate-determining step in the reaction mechanism for the two calculations, DFT and Matlantis.

Regarding the proposed reaction mechanism and the existence of neighbor O vacancies, there are high-resolution transmission spectroscopy results showing that the etching process can generate defects in MXenes, with patches of defective surface groups.[50,51] Therefore, the proposal of the reaction mechanism requiring two neighbor sites appears to be reasonable.

Conclusions

There are currently over 70 MXenes reported in the literature. Due to their conducting/semiconducting properties, many studies have reported on the use of MXenes as electrocatalysts or in photocatalysis. In comparison, the activity of MXenes as thermal catalysts still remains almost unexplored, offering a vast potential for innovation since these materials offer the possibility of tuning the electronic properties of the metal and controlling the nature of the surface functional groups. Herein,
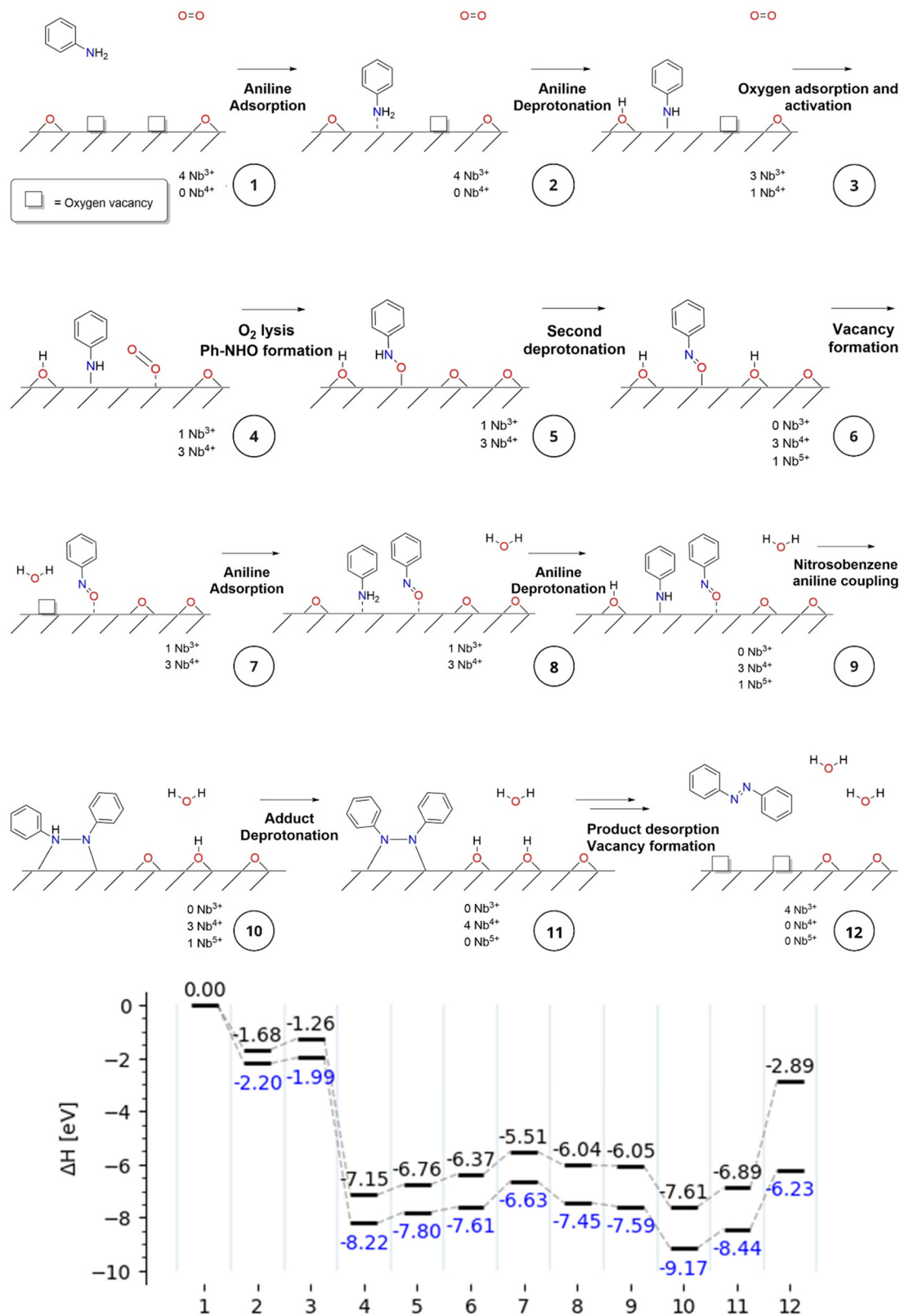
Fig. 7 Proposed reaction mechanism of the aniline oxidative coupling reaction with Nb_2CO_2 MXene as the catalyst (top). Reaction energy profile of the reaction intermediates provided by CASTEP DFT (black) and Matlantis (blue) codes (bottom).

we report the catalytic activity of Nb$_2$C MXene as a bifunctional acid–base solid, efficiently promoting the aldolic condensation. Considering the low density of the acidic and basic sites measured by NH$_3$- and CO$_2$-TPD, the TOF values achieved by Nb$_2$C MXene in the aldolic condensation are remarkable and much higher than those of reference solid acids and bases. It is proposed that this high activity arises from the bifunctional acid–base nature of Nb$_2$C MXene, and the appropriate strength of the sites that depend on the work function and collective electron density on the MXene. It was found that Nb$_2$C MXene can promote aerobic oxidation of aniline to azo- and azoxy-benzene. Furthermore, Nb$_2$C MXene acted as a hydrogenation catalyst with 100% selectivity towards azobenzene when a hydrogenation step was implemented after the oxidative aniline coupling. Theoretical calculations indicate that the active sites require cooperation of two neighbor O vacancies to achieve the coupling.

Overall, the present results bring attention to the need for a systematic study of the thermo-catalytic properties of MXenes to try to understand the nature of the sites, and to develop possible tools that can tune their electronic properties and increase the population of these sites, showing the advantages that these 2D nanomaterials can offer in comparison with the current benchmark catalysts.

Data availability

Data are available from the corresponding authors upon reasonable request and Zenodo repository.

Conflicts of interest

There are no conflicts to declare.

Acknowledgements

References

1 M. Naguib, M. W. Barsoum and Y. Gogotsi, *Adv. Mater.*, 2021, **33**, 2103393.
2 I. Persson, L.-Å. Näslund, J. Halim, M. W. Barsoum, V. Darakchieva, J. Palisaitis, J. Rosen and P. O. Å. Persson, *2D Mater.*, 2017, **5**, 015002.
3 J. Huang, Z. Li, Y. Mao and Z. Li, *Nano Select*, 2021, **2**, 1480–1508.
4 H. Kim, Z. Wang and H. N. Alshareef, *Nano Energy*, 2019, **60**, 179–197.
5 Y. Sun and Y. Li, *Chemosphere*, 2021, **271**, 129578.
6 S. G. Peera, C. Liu, A. K. Sahu, M. Selvaraj, M. Rao, T. G. Lee, R. Koutavarapu, J. Shim and L. Singh, *Adv. Mater. Interfaces*, 2021, **8**, 2100975.
7 S. Bai, M. Yang, J. Jiang, X. He, J. Zou, Z. Xiong, G. Liao and S. Liu, *npj 2D Mater. Appl.*, 2021, **5**, 78.
8 H. Wang and J.-M. Lee, *J. Mater. Chem. A*, 2020, **8**, 10604–10624.
9 H. T. Das, T. E. Balaji, S. Dutta, N. Das and T. Maiyalagan, *Int. J. Energy Res.*, 2022, **46**, 8625–8656.
10 Y. Sun, X. Meng, Y. Dall'Agnese, C. Dall'Agnese, S. Duan, Y. Gao, G. Chen and X.-F. Wang, *Nano-Micro Lett.*, 2019, **11**, 1–22.
11 Z. Guo, Y. Li, B. Sa, Y. Fang, J. Lin, Y. Huang, C. Tang, J. Zhou, N. Miao and Z. Sun, *Appl. Surf. Sci.*, 2020, **521**, 146436.
12 A. Morales-Garcia, F. Calle-Vallejo and F. Illas, *ACS Catal.*, 2020, **10**, 13487–13503.
13 N. H. Ahmad Junaidi, W. Y. Wong, K. S. Loh, S. Rahman and W. R. W. Daud, *Int. J. Energy Res.*, 2021, **45**, 15760–15782.
14 M. Zhang, C. Lai, B. Li, S. Liu, D. Huang, F. Xu, X. Liu, L. Qin, Y. Fu and L. Li, *Small*, 2021, **17**, 2007113.
15 W. Kong, J. Deng and L. Li, *J. Mater. Chem. A*, 2022, **10**, 14674–14691.
16 Y. Yang, Y. Xu, Q. Li, Y. Zhang and H. Zhou, *J. Mater. Chem. A*, 2022, **10**, 19444–19465.
17 X. Zhang, Y. Li, C. Qian, L. An, W. Wang, X. Li, X. Shao and Z. Li, *RSC Adv.*, 2023, **13**, 9466–9478.
18 M. Climent, A. Corma, V. Fornés, R. Guil-Lopez and S. Iborra, *Adv. Synth. Catal.*, 2002, **344**, 1090–1096.
19 B. de Campos Ventura-Camargo and M. A. Marin-Morales, *Text. Light Indust. Sci. Technol.*, 2013, **2**, 85–103.
20 K. Yamjala, M. S. Nainar and N. R. Ramisetti, *Food Chem.*, 2016, **192**, 813–824.
21 R. M. Christie and J. L. Mackay, *Color. Technol.*, 2008, **124**, 133–144.
22 K. G. Yager and C. J. Barrett, *Azobenzene polymers as photomechanical and multifunctional smart materials*, RSC Publishing, Cambridge, UK, 2008.
23 D. H. Reneker, W. L. Mattice, R. P. Quirk and S. Kim, *Smart Mater. Struct.*, 1992, **1**, 84.
24 E. Merino, *Chem. Soc. Rev.*, 2011, **40**, 3835–3853.
25 A. Grirrane, A. Corma and H. García, *Science*, 2008, **322**, 1661–1664.
26 A. Grirrane, A. Corma and H. Garcia, *Nat. Protoc.*, 2010, **5**, 429–438.

27 X. Liu, H. Q. Li, S. Ye, Y. M. Liu, H. Y. He and Y. Cao, *Angew. Chem., Int. Ed.*, 2014, **53**, 7624–7628.

28 C. Peng, P. Wei, X. Chen, Y. Zhang, F. Zhu, Y. Cao, H. Wang, H. Yu and F. Peng, *Ceram. Int.*, 2018, **44**, 18886–18893.

29 S. Gul, M. I. Serna, S. A. Zahra, N. Arif, M. Iqbal, D. Akinwande and S. Rizwan, *Surf. Interfaces*, 2021, **24**, 101074.

30 P. Montes-Navajas, N. G. Asenjo, R. Santamaría, R. Menendez, A. Corma and H. García, *Langmuir*, 2013, **29**, 13443–13448.

31 R. Ramírez Grau, A. Lewandowska-Andralojc, A. Primo and H. García, *Int. J. Hydrogen Energy*, 2023, **48**(53), 20314–20323.

32 S.-M. Lam, Z. H. Jaffari, Y.-T. Ong, J.-C. Sin, H. Lin, H. Li and H. Zeng, *Toxic Gas Sens. Biosens.*, 2021, **92**, 107–138.

33 H. Zhou, Z. Chen, E. Kountoupi, A. Tsoukalou, P. M. Abdala, P. Florian, A. Fedorov and C. R. Müller, *Nat. Commun.*, 2021, **12**, 1–10.

34 M.-C. Liu, B.-M. Zhang, Y.-S. Zhang, D.-T. Zhang, C.-Y. Tian, L.-B. Kong and Y.-X. Hu, *Batteries Supercaps*, 2021, **4**, 1473–1481.

35 K. Arole, J. W. Blivin, A. M. Bruce, S. Athavale, I. J. Echols, H. Cao, Z. Tan, M. Radovic, J. L. Lutkenhaus and M. J. Green, *Chem. Commun.*, 2022, **58**, 10202–10205.

36 T. Su, R. Peng, Z. D. Hood, M. Naguib, I. N. Ivanov, J. K. Keum, Z. Qin, Z. Guo and Z. Wu, *ChemSusChem*, 2018, **11**, 688–699.

37 S. Huang and V. N. Mochalin, *ACS Nano*, 2020, **14**, 10251–10257.

38 A. Sarycheva and Y. Gogotsi, *Chem. Mater.*, 2020, **32**, 3480–3488.

39 V. Presser, M. Naguib, L. Chaput, A. Togo, G. Hug and M. W. Barsoum, *J. Raman Spectrosc.*, 2012, **43**, 168–172.

40 J. Halim, K. M. Cook, M. Naguib, P. Eklund, Y. Gogotsi, J. Rosen and M. W. Barsoum, *Appl. Surf. Sci.*, 2016, **362**, 406–417.

41 C. Zhang, M. Beidaghi, M. Naguib, M. R. Lukatskaya, M.-Q. Zhao, B. Dyatkin, K. M. Cook, S. J. Kim, B. Eng and X. Xiao, *Chem. Mater.*, 2016, **28**, 3937–3943.

42 D. Ponnalagar, D.-R. Hang, S. E. Islam, C.-T. Liang and M. M. Chou, *Mater. Des.*, 2023, 112046.

43 A. Corma, *Chem. Rev.*, 1997, **97**, 2373–2420.

44 M. a J. Climent, A. Corma, S. Iborra and A. Velty, *J. Mol. Catal. A: Chem.*, 2002, **182**, 327–342.

45 R. Mestres, *Green Chem.*, 2004, **6**, 583–603.

46 Q. Liu, C. Zhang, N. Shi, X. Zhang, C. Wang and L. Ma, *RSC Adv.*, 2018, **8**, 13686–13696.

47 S. Han, Y. Cheng, S. Liu, C. Tao, A. Wang, W. Wei, H. Yu and Y. Wei, *Angew. Chem.*, 2021, **133**, 6452–6455.

48 I. J. Echols, D. E. Holta, V. S. Kotasthane, Z. Tan, M. Radovic, J. L. Lutkenhaus and M. J. Green, *J. Phys. Chem. C*, 2021, **125**, 13990–13996.

49 X. Hong, Z. Xu, Z. P. Lv, Z. Lin, M. Ahmadi, L. Cui, V. Liljeström, V. Dudko, J. Sheng and X. Cui, *Adv. Sci.*, 2024, **11**, 2305099.

50 Y. Tang, C. Yang, X. Xu, Y. Kang, J. Henzie, W. Que and Y. Yamauchi, *Adv. Energy Mater.*, 2022, **12**, 2103867.

51 F. Zhan, G. Wen, R. Li, C. Feng, Y. Liu, Y. Liu, M. Zhu, Y. Zheng, Y. Zhao and P. La, *Phys. Chem. Chem. Phys.*, 2024, **26**, 11182–11207.